ELSEVIER

Contents lists available at ScienceDirect

Journal of Power Sources

journal homepage: www.elsevier.com/locate/jpowsour





Enhancing cycling performance of all-solid-state lithium batteries using Li_{6.4}La_{3.0}Zr_{2.0}Al_{0.2}O₁₂-reinforced hybrid solid electrolyte

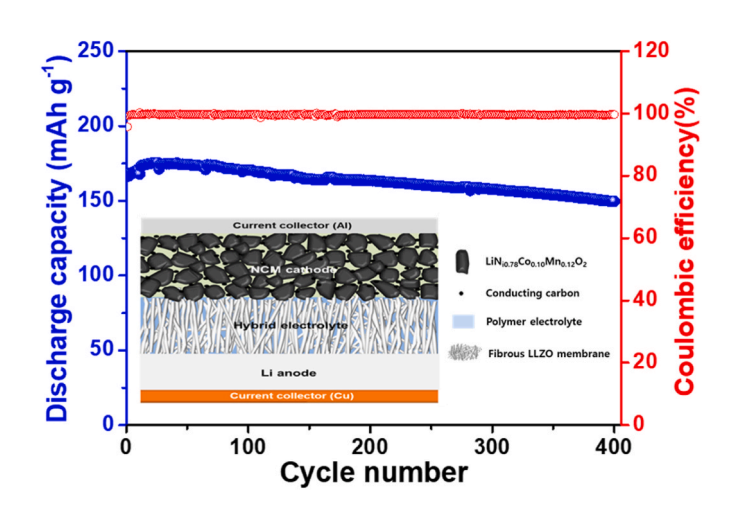
Lei Wu Tian a,b, Ji Wan Kim a,c,** Dongmei Xie a, Weihan Li b,* Dong-Won Kim a,c,** Dong-Won Kim a,c,**

- ^a Department of Chemical Engineering, Hanyang University, Seoul, 04763, South Korea
- b Ningbo Key Laboratory of All-Solid-State Battery, Eastern Institute for Advanced Study, Eastern Institute of Technology, Ningbo, Zhejiang, 315201, China
- ^c Department of Battery Engineering, Hanyang University, Seoul, 04763, South Korea

HIGHLIGHTS

- A hybrid electrolyte with LLZAO membrane enhances ionic conductivity and robustness.
- The Li/NCM cell with hybrid electrolyte showed excellent cycling stability.
- The LLZAO-based hybrid electrolytes offer high safety and performance for ASSI Be

GRAPHICAL ABSTRACT



ARTICLE INFO

Keywords: Solid hybrid electrolytes LLZAO membrane All-solid-state batteries Ionic conductivity Cycle performance

ABSTRACT

All-solid-state lithium batteries (ASSLBs) utilizing solid electrolytes are regarded as highly promising candidates for next-generation batteries due to their high energy density and enhanced safety. However, technical challenges such as low ionic conductivity and interfacial issues of solid electrolytes currently restrict the practical applications of ASSLBs. In this study, solid hybrid electrolytes are developed by incorporating a polymer electrolyte composed of poly(vinylidene fluoride-co-hexafluoropropylene), poly(ϵ -caprolactone), 1-propyl-1-methyl-pyrrolidinium bis(trifluoromethylsulfonyl)imide, and lithium bis (trifluoromethanesulfonyl)imide into a fibrous Li_{6.4}La_{3.0}Zr_{2.0}Al_{0.2}O₁₂ (LLZAO) membrane. The incorporation of an ion-conductive fibrous LLZAO membrane with the polymer electrolyte significantly enhances mechanical robustness and achieves a high ionic conductivity. The Li/LiNi_{0.78}Co_{0.10}Mn_{0.12}O₂ cell employing this solid hybrid electrolyte delivers a high discharge capacity of 198.3 mAh g⁻¹ at 0.1C and 55 °C, exhibits an excellent cycling retention of 89.0 % at 400th cycle at

^{*} Corresponding author.

^{**} Corresponding author. Department of Chemical Engineering, Hanyang University, Seoul, 04763, South Korea. E-mail addresses: whli@eitech.edu.cn (W. Li), dongwonkim@hanyang.ac.kr (D.-W. Kim).

1. Introduction

Lithium metal has emerged as a highly attractive anode material for advanced lithium batteries due to its impressive specific capacity (3860 mAh $\rm g^{-1}$) and low electrochemical potential (-3.040 V vs. SHE) [1,2]. Despite these advantages, the practical application of lithium metal anodes in liquid electrolyte-based batteries faces technical challenges, primarily concerning safety and capacity fading during repeated cycling [3]. These issues predominantly arise from uncontrolled lithium dendrite growth and undesirable side reactions with liquid electrolytes. In contrast, solid electrolytes can effectively suppress both dendrite growth and electrolyte-related side reactions during cycling. Moreover, solid electrolytes mitigate the safety risks associated with flammable liquid electrolytes, offering the potential for lithium anodes to attain higher energy densities compared to graphite-based lithium-ion batteries [4,5].

Solid electrolytes are categorized into two main types: inorganic electrolytes and polymer electrolytes. Inorganic electrolytes such as $\text{Li}_7\text{La}_3\text{Zr}_2\text{O}_{12}$ (LLZO), $\text{Li}_{0.3}\text{La}_{0.557}\text{TiO}_3$ (LLTO), $\text{Li}_6\text{PS}_5\text{Cl}$, and $\text{Li}_{10}\text{GeP}_2\text{S}_{12}$ are well known for their high ion conductivity, mechanical robustness, and excellent thermal stability [6–9]. However, their inherent rigidity and brittleness pose challenges in achieving good interfacial stability with electrodes during cycling [10]. In contrast, solid polymer electrolytes offer flexibility, film formability and elasticity, which facilitate intimate contact at the electrolyte-electrode interface [11–15]. Despite these advantages, solid polymer electrolytes suffer from low ionic conductivities, limited mechanical strength, and poor electrochemical stability [12,16].

The formulation of solid hybrid electrolytes represents a highly promising strategy for advancing all-solid-state lithium batteries (ASSLBs) [17–19]. This approach has the potential to not only improve ionic conductivity but also enhance mechanical strength while retaining flexibility of the electrolyte [20-22]. Wang et al. prepared vertically aligned Li₇La₃Zr₂O₁₂ sheet arrays and employed them to fabricate a composite solid electrolyte with a thickness of 8 µm [20]. The resulting electrolyte exhibited a room-temperature ionic conductivity of 2.6 \times 10⁻⁴ S cm⁻¹. The superior Li-ion conduction and enhanced mechanical strength stabilized Li plating/stripping behavior, enabling the symmetric Li cell to operate for over 1200 h at 1.0 mA cm $^{-2}$ and 60 °C. Ma et al. prepared powdery three-dimensional hexagonal boron nitride (3D h-BN) and incorporated it into poly(ethylene oxide) (PEO)-based electrolytes [23]. The addition of 5 wt% 3D h-BN significantly enhanced the ionic conductivity (8.9 $\times~10^{-4}~S~cm^{-1}$ at 60 $^{\circ}\text{C})$ and mechanical strength. A discharge capacity of 138.9 mAh g⁻¹ was recorded for the Li/LiFePO₄ cell incorporating the hybrid electrolyte, with 89 % capacity retention observed after 100 cycles at 1C. Nevertheless, most solid hybrid electrolytes reported to date still suffer from low ionic conductivity and high interfacial resistance due to interfacial instability [15,24, 25].

In the present work, a solid hybrid electrolyte was designed and evaluated by incorporating a polymer electrolyte into the fibrous $\text{Li}_{6.4}\text{La}_{3.0}\text{Zr}_{2.0}\text{Al}_{0.2}\text{O}_{12}$ (LLZAO) membrane. The polymer electrolyte consisting of poly(vinylidene fluoride-co-hexafluoropropylene) (PVdF-HFP), poly(ϵ -caprolactone) (PCL), 1-propyl-1-methyl pyrrolidinium bis (trifluoromethylsulfonyl)imide (Pyr $_{13}$ -TFSI) as an ionic liquid plasticizer, and lithium bis(trifluoromethanesulfonyl)imide (LiTFSI), serves as a flexible and highly adhesive ion conductor. To improve ionic conductivity and minimize interfacial resistance at the electrode–electrolyte interface, PCL and Pyr $_{13}$ -TFSI were incorporated into the polymer electrolyte [26–31]. The fibrous LLZAO membrane was chosen as the framework because it offers continuous Li^+ conduction pathways,

excellent resistance to oxidative decomposition, and superior mechanical and thermal stability. For the polymer components, PCL was selected due to its relatively high ionic conductivity and wide electrochemical stability window, enabling compatibility with high-voltage cathodes. On the other hand, PVdF-HFP offers complementary advantages, including excellent chemical and electrochemical stability, outstanding film-forming ability, mechanical flexibility, and high oxidative resistance, which collectively enhance interfacial contact and ensure safe operation. The obtained hybrid electrolyte demonstrated high ionic conductivity, superior interfacial behavior with the lithium electrode, and enhanced electrochemical stability. These characteristics facilitated stable operation of a symmetric Li cell for more than 1000 h at 0.6 mA cm⁻². Furthermore, a solid-state Li/LiNi_{0.78}Co_{0.10}Mn_{0.12}O₂ (NCM) cell employing this hybrid electrolyte delivered a high discharge capacity and demonstrated excellent capacity retention of 89.0 % after 400 cycles at 0.5C and 55 °C. Additionally, the LLZAO-based hybrid electrolyte exhibited a high thermal stability without short-circuit at 160 °C. Therefore, the solid hybrid electrolyte developed in this study shows great promise for enhancing the cycling performance and thermal stability of ASSLBs.

2. Experimental section

2.1. Preparation of solid hybrid electrolytes

The fibrous LLZAO membrane was fabricated using the electrospinning method. The precursor was prepared by dissolving LiNO₃ (Sigma Aldrich, 99 %), La(NO₃)₃·6H₂O (Sigma Aldrich, 99.99 %), C₈H₁₂O₈Zr (Zr content: 15.0–16.0 %, Sigma Aldrich), Al(NO₃)₃·9H₂O (Sigma Aldrich, 99 %) in a mixed solvent composed of 85 wt% water and 15 wt% acetic acid. Poly(vinyl pyrrolidone) was then introduced into the solution, and the mixture was magnetically stirred for 24 h to yield transparent electrospinning solution. A voltage of 15 kV was applied using a high-voltage power amplifier. The needle-to-collector distance and roller speed were set to 17 cm and 200 rpm, respectively. After electrospinning, the fibrous membrane deposited on aluminum foil was dried in a vacuum oven at 60 °C for 2 h, followed by calcination in air at 700 °C for 3 h with a heating rate of 2 °C min⁻¹. The resulting LLZAO membrane was then collected and transferred to a glove box for further experiments. The polymer electrolyte solution was prepared by dissolving PCL (M_n: 80,000 g mol⁻¹, Sigma-Aldrich), PVdF-HFP (Kynar 2801, M_w : 4.77 \times 10⁵ g mol⁻¹, Arkema), Pyr₁₃-TFSI (Solvionic), and LiTFSI (Sigma-Aldrich) in a mixed solvent of acetone and tetrahydrofuran (1:2 by volume), followed by stirring for 5 h. The resulting solution was cast onto the porous LLZAO membrane to facilitate infiltration. It was dried in the glove box for 5 h at room temperature and further subjected to vacuum drying at 80 °C for 12 h.

2.2. Electrode and cell fabrication

The cathode slurry was obtained through the mixing of 84 wt% LiNi $_{0.78}$ Co $_{0.10}$ Mn $_{0.12}$ O $_{2}$ (NCM, L&F Co., Ltd.), 5 wt% poly(vinylidene fluoride) (PVdF, Solef 5130, Solvay), 5 wt% Super P (Timcal), 5 wt% succinonitrile (SN, Sigma-Aldrich), and 1 wt% LiTFSI in N-methyl-2-pyrrolidone. NCM consists of single-crystalline particles with an average size of 4.6 μ m, as shown in Fig. S1. After casting the slurry onto carbon-coated Al foil, it was dried under vacuum conditions at 80 °C for 24 h. As the anode, a 200 μ m-thick lithium metal (Honjo Metal Co., Ltd.) supported by a copper foil was employed. The Li/solid hybrid electrolyte/NCM cells were fabricated inside an argon-filled glove box (MBRAUN), where both H₂O and O₂ levels were strictly controlled to remain below

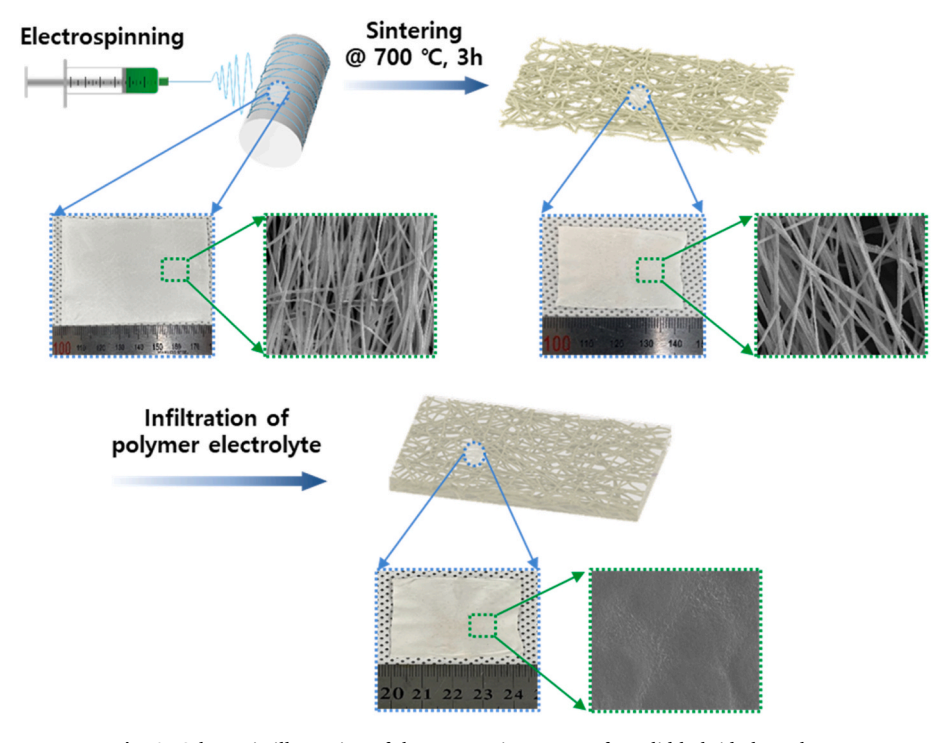


Fig. 1. Schematic illustration of the preparation process for solid hybrid electrolyte.

0.1 ppm.

2.3. Characterization and measurements

Field-emission scanning electron microscopy (FE-SEM; Verios G4 UC, FEI) was employed to observe the surface morphologies of the samples. The crystalline structures of the LLZAO membrane and hybrid electrolyte were characterized by X-ray diffraction using Cu Kα radiation on a D8 ADVANCE (Bruker) instrument. To investigate thermal stability, the solid electrolytes were subjected to thermogravimetric analysis in an air atmosphere from 25 to 800 °C. Differential scanning calorimetry (DSC, TA Instruments) was performed to investigate the thermal properties of the samples at a heating rate of 10 $^{\circ}$ C min $^{-1}$. Surface chemical species formed on the lithium anode after cycling were identified using X-ray photoelectron spectroscopy (XPS, K-alpha, Thermo Scientific). To analyze the composition of the solid electrolyte interphase (SEI) formed on the lithium metal anode, time-of-flight secondary ion mass spectrometry (ToF-SIMS) was conducted. Solid-state magic angle spinning (MAS) ⁷Li nuclear magnetic resonance (NMR) spectra were recorded using a Bruker AVANCE III 400 spectrometer equipped with a 1.9 mm HX-MAS probe, operating at a spinning rate of 25 kHz. Solid LiCl was used as a reference for the ⁷Li chemical shift, set at 0 ppm. To determine the ionic conductivity, a symmetric stainless steel (SS)/solid electrolyte/ SS cell was constructed, and ac impedance measurements were conducted using electrochemical impedance spectroscopy (EIS) over a frequency range of 1 MHz to 1 Hz with an amplitude of 10 mV. The oxidative stability of the solid electrolyte was assessed by linear sweep voltammetry (LSV) at 55 °C and 1 mV s⁻¹. Cycling stability at the lithium metal interface was examined through galvanostatic plating/ stripping of lithium in a symmetric Li/solid electrolyte/Li cell. The Li/ solid electrolyte/NCM cells were tested over a voltage range of 3.0-4.2 V at 25 $^{\circ}\text{C}$ and 55 $^{\circ}\text{C}$ using a WBSC3000 battery cycler.

3. Results and discussion

To optimize the content of the ionic liquid (IL), Pyr_{13} -TFSI, in the polymer electrolyte, ionic conductivity was measured while varying the IL content from 0 to 60 wt%. In these compositions, the mass ratio of

PVdF-HFP to LiTFSI was fixed at 2:1. Fig. S2a shows the ionic conductivities of the polymer electrolytes as a function of IL content at 25 °C. Without IL, the ionic conductivity was very low $(1.3 \times 10^{-7} \text{ S cm}^{-1})$. As the IL content increased, the ionic conductivity gradually increased, reaching $0.95 \times 10^{-4} \text{ S cm}^{-1}$ at 60 wt%. To analyze the conductivity trends, we estimated the slope of the log σ vs. IL content plot. In the low-IL region (0–10 wt%), the slope is steep, whereas in the higher IL content range (10-60 wt%), it significantly decreases. This behavior indicates that once a sufficient amount of IL is incorporated to disrupt polymer crystallinity and lower the Li+ migration barrier, further IL addition simultaneously lowers the migration barrier and increases the carrier concentration. However, a free-standing film could not be obtained when the IL content exceeded 60 wt%. Therefore, the optimal Pyr_{13} -TFSI content was set at 60 wt% considering both ionic conductivity and mechanical integrity of polymer electrolyte. Since the ionic conductivity of the polymer electrolyte was not sufficiently high, ion conductive polymer (PCL) was added in place of PVdF-HFP in the previous composition. Fig. S2b presents the variation in the ionic conductivity of polymer electrolytes with different contents of PCL in the polymer matrix (PCL and PVdF-HFP). The ionic conductivity increases with higher PCL content, which can be attributed to enhanced salt solvation and ion transport facilitated by the flexible ester chains in PCL [32]. However, when the PCL content reached 75 wt%, the polymer electrolyte lost its self-standing property. Therefore, the optimum PCL content was determined to be 50 wt%. Based on these results, the optimal composition ratio of PCL: PVdF-HFP: Pyr₁₃-TFSI was set at 1:1:3 based on weight, and the resulting electrolyte material is referred to as the "polymer electrolyte" in the following sections.

The hybrid electrolyte was prepared through a sequential process involving electrospinning, sintering, and infiltration of the polymer electrolyte, as schematically illustrated in Fig. 1. First, a fibrous membrane composed of polymer and salts was fabricated using the electrospinning method [33,34]. The LLZAO membrane was fabricated by sintering the polymer/salt precursor membrane at 700 °C for 3 h in a muffle furnace. Preparation of the solid hybrid electrolyte involved impregnating the fibrous LLZAO scaffold with the polymer electrolyte solution and subsequently drying it to eliminate residual solvent.

The morphology of the electrospun polymer/salt nanofibrous

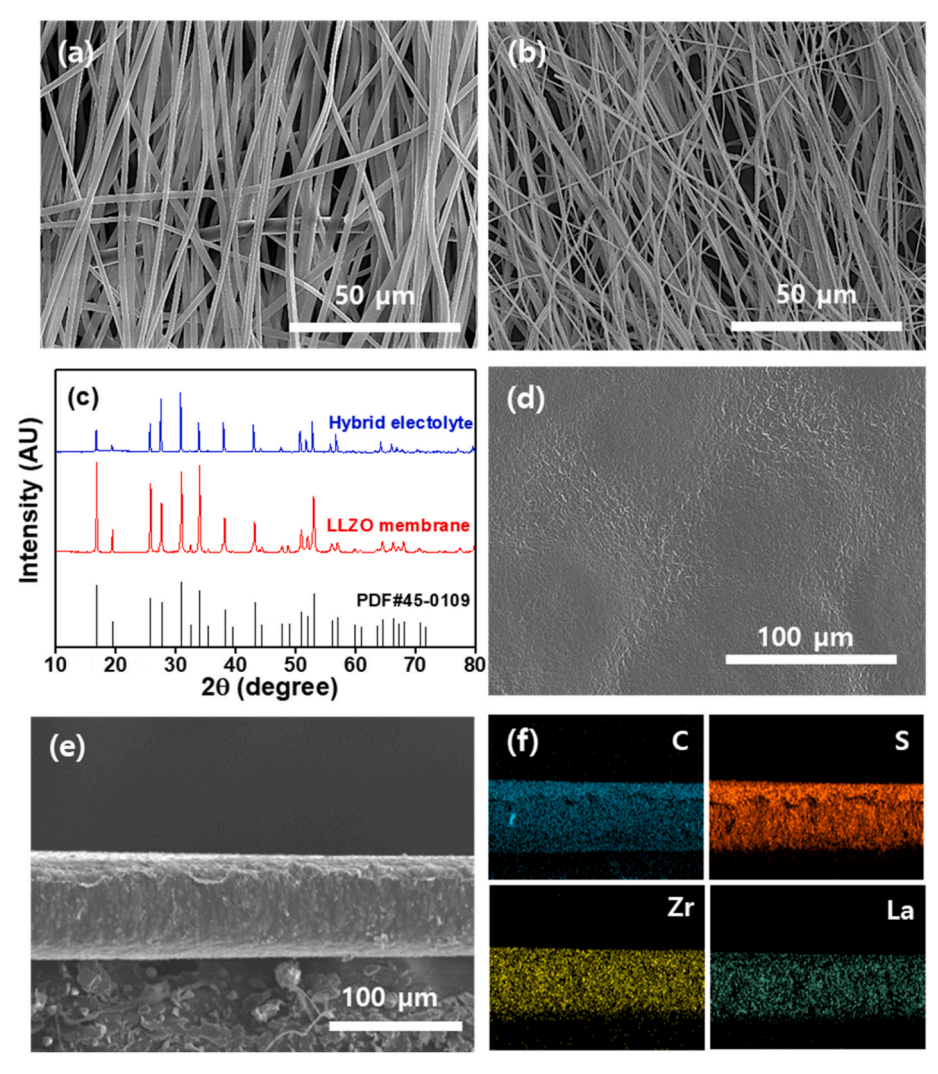


Fig. 2. SEM images of (a) the LLZAO precursor and (b) the sintered LLZAO membrane. (c) XRD patterns comparing the LLZAO membrane and the hybrid electrolyte. (d) Top-view and (e) cross-sectional SEM images, along with (f) elemental distribution mapping of the hybrid electrolyte.

membrane is shown in Fig. 2a, revealing a highly porous structure with an average fiber diameter of approximately 1.5 µm. The porosity of the LLZAO membrane was determined to be 80 %. The sintering treatment resulted in a reduction of the LLZAO nanofiber diameter to an average of 750 nm (Fig. 2b). The resulting LLZAO membrane forms a continuous fibrous structure, which provides the effective pathways for lithium-ion conduction and enhances mechanical integrity. ICP-OES analysis was conducted to determine the elemental composition of LLZAO, and the measured result ($L_{6.44}La_{3.02}Zr_{1.97}Al_{0.19}O_{12}$) confirms the successful synthesis of $Li_{6.4}La_{3.0}Zr_{2.0}Al_{0.2}O_{12}$. Fig. 2c presents the XRD results for both the LLZAO membrane and the hybrid electrolyte. The XRD pattern of the LLZAO membrane shows characteristic peaks corresponding to the cubic-phase garnet (PDF#45-0109) [35], which has been commonly used as a model for studying the garnet-type structure of LLZAO materials. The diffraction peaks of the hybrid electrolyte (LLZAO membrane filled with polymer electrolyte) show no noticeable shift compared to those of the LLZAO membrane, suggesting chemical compatibility among the components in the hybrid electrolyte. After carefully optimizing the mechanical properties, we selected an LLZAO framework with a thickness of 70 μm , which enabled the fabrication of a robust hybrid electrolyte. When the LLZAO membrane thickness was reduced below 70 μm , the framework became too fragile, making it difficult to obtain a flexible hybrid electrolyte. Fig. 2d and e shows the top-view and cross-sectional SEM images of the hybrid electrolyte. The hybrid

electrolyte reveals a flat and densely structured surface, demonstrating that the polymer electrolyte has completely occupied the pores of the LLZAO membrane. This is further supported by cross-sectional image, which shows a dense structure without observable voids or pores. Elemental mappings of C, S, Zr, La, and Al in Fig. 2f and S3 reveal a uniform distribution of these elements throughout the hybrid electrolyte. Through pore filling by the polymer electrolyte, a dense 70 μm-thick uniform hybrid electrolyte film was successfully produced. In the hybrid electrolyte, the mass ratio of LLZAO was approximately 37.8 %. At this composition, the LLZAO framework provides continuous Li⁺ ion conduction pathways and mechanical reinforcement, while the polymer phase contributes flexibility, interfacial adhesion, and film processability. We found that increasing the LLZAO content beyond this level enhanced the ionic conductivity but caused brittleness. Conversely, reducing the LLZAO content improves flexibility but compromises ionic conductivity. Therefore, the optimized value of LLZAO contents represents a balanced composition, achieving both high ionic conductivity and robust mechanical/electrochemical properties.

The hybrid and polymer electrolytes were characterized for their ionic conductivities across temperatures ranging from 25 to 75 °C, as shown in Fig. 3a. At 25 °C, the polymer electrolyte showed an ionic conductivity of $1.4 \times 10^{-4} \, \mathrm{S \, cm^{-1}}$. This value increased to $2.7 \times 10^{-4} \, \mathrm{S \, cm^{-1}}$ upon incorporation of the polymer electrolyte into the LLZAO membrane. The presence of LLZAO fibers is responsible for the improved

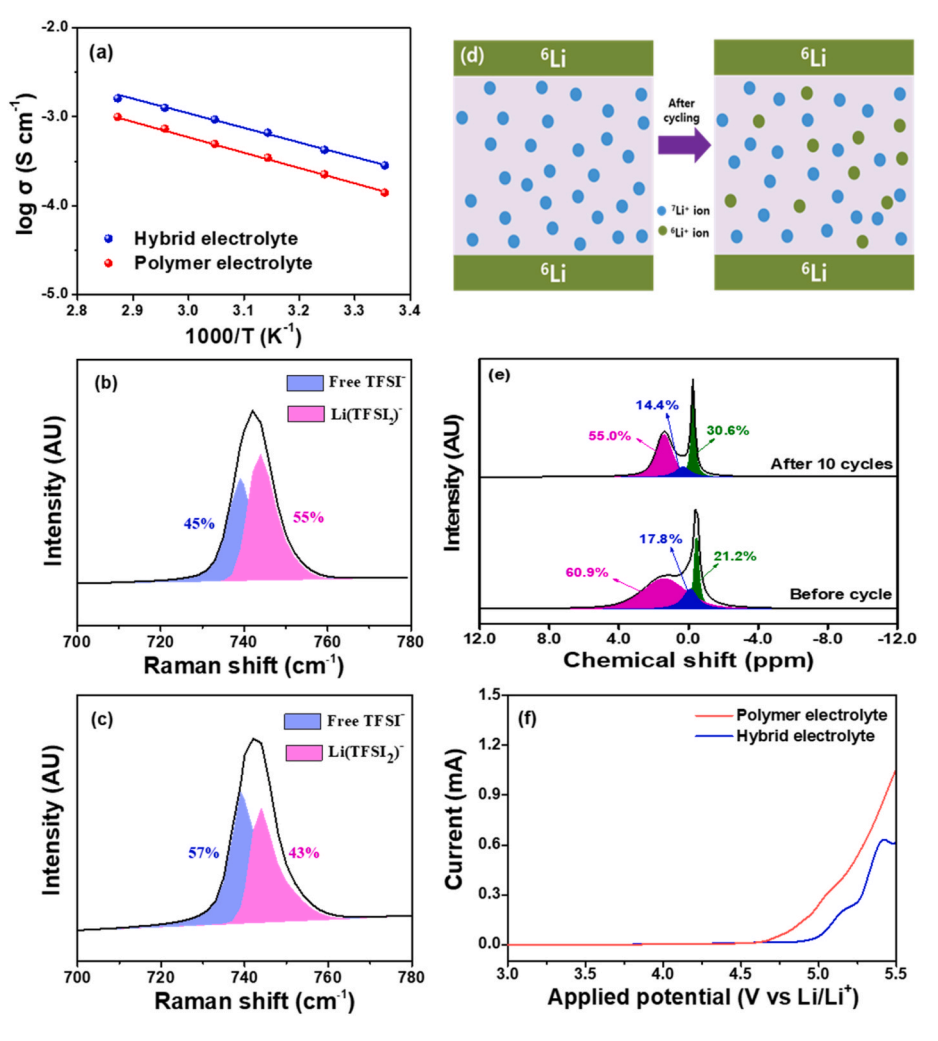


Fig. 3. (a) Variation in ionic conductivity of different solid electrolytes with temperature. Deconvoluted Raman spectra of (b) polymer electrolyte and (c) hybrid electrolyte in the wavenumber range of 700–780 cm⁻¹. (d) Substitution of ⁷Li ⁺ ions with ⁶Li ⁺ ions due to the conduction of ⁶Li ⁺ ions in the ⁶Li/hybrid electrolyte/⁶Li cell. (e) Deconvoluted ⁷Li NMR spectra of hybrid electrolyte before and after 10 cycles in the ⁶Li symmetric cell. (f) Linear sweep voltammograms of solid electrolytes at 1 mV s⁻¹.

ionic conductivity of the hybrid electrolyte, which facilitate lithium-ion transport by offering efficient ion-conduction pathways [36,37], Fig. S4 shows the DSC thermograms of PVdF-HFP, the polymer electrolyte, and the hybrid electrolyte. PVdF-HFP exhibited a melting temperature (T_m) of 147.1 °C. Both the melting temperature and the heat of fusion were reduced in the polymer and hybrid electrolytes compared with pristine PVdF-HFP, indicating that the incorporation of the ionic liquid, lithium salt, and LLZAO decreases the crystallinity of PVdF-HFP, thereby enhancing the ionic conductivity of the hybrid electrolyte. In the hybrid electrolyte, the LLZAO membrane could facilitate lithium salt dissociation, thereby increasing the concentration of free Li + ions. This presumption was supported by Raman spectra in Fig. 3b and c. The C-N-C bending vibration of the TFSI⁻ anion in the 735 - 750 cm⁻¹ region exhibits two characteristic peaks: one at \sim 739 cm⁻¹ corresponding to free TFSI⁻, and another at \sim 745 cm⁻¹ assigned to ion clusters ([Li(TFSI)₂]⁻) [38,39]. Deconvolution of these peaks revealed that the fraction of free TFSI was 57.0 % in the hybrid electrolyte, which is much higher than the 45.0 % observed in the polymer electrolyte. This result indicates that the LLZAO surface facilitates the dissociation of LiTFSI, thereby suppressing ion-pair aggregation. To better understand ion transport characteristics within the hybrid electrolyte, solid-state ⁷Li MAS NMR spectra were acquired before and after its subjection to galvanostatic stripping/deposition cycles in a symmetric ⁶Li/hybrid electrolyte/⁶Li cell at 0.1 mA cm⁻² for 2 h (Fig. 3d). As depicted in Fig. 3e, three distinct peaks corresponding to different Li⁺ environments could be identified by deconvoluting the asymmetric peak in the NMR spectra. These peaks correspond to Li⁺ ions in the LLZAO fibers (1.09 ppm), at the LLZAO-polymer electrolyte interface (-0.20 ppm), and within the polymer electrolyte (-0.44 ppm) [40-42]. Before cycling, the mobile Li⁺ population was predominantly located in LLZAO, accounting for 60.9 %. After cycling of the ⁶Li/hybrid electrolyte/⁶Li cell, the Li⁺ population in LLZAO and at the LLZAO-polymer interface decreased to 55.0 % and 14.4 %, respectively. This is because some ^7Li $^+$ ions in LLZAO and at interface are replaced with ⁶Li ⁺ ions during cycling in the ⁶Li/hybrid electrolyte/⁶Li cell. The relative population changes after cycling indicate that Li + ions migrate more favorably through the LLZAO fibers and interfacial regions, which are expected to present lower transport energy barriers compared to the polymer electrolyte. As previously discussed, Raman analysis (Fig. 3b and c) revealed a higher fraction of free TFSI in the hybrid electrolyte than in the polymer electrolyte, which increases the concentration of mobile Li⁺ ions and complements the preferential Li⁺ conduction along the grain boundaries of LLZAO. These results suggest that Li⁺ ions preferentially transport through the interconnected LLZAO fibers and the LLZAO-polymer electrolyte interface due to the lower transport energy barrier in these regions. Fig. 3f presents the results of linear sweep voltammetry, which was conducted at a scan rate of 1 mV s⁻¹ to investigate the electrochemical stability of the prepared solid electrolytes. The linear sweep

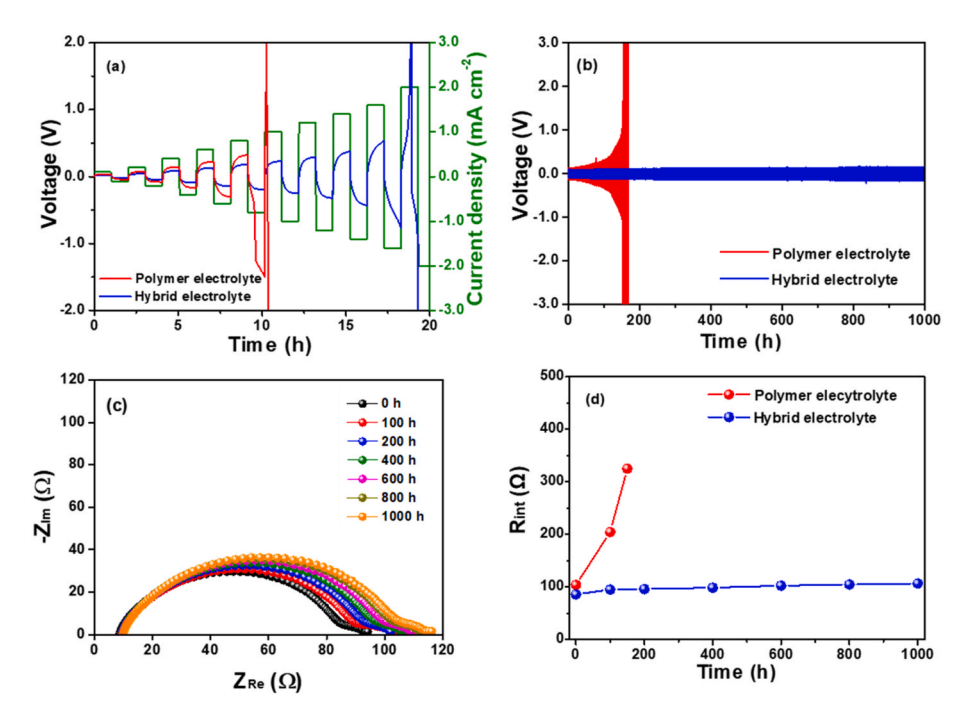


Fig. 4. (a) Galvanostatic cycling curves of symmetric Li/Li cells employing polymer and hybrid electrolytes under stepwise-increased current densities at 55 °C. (b) Voltage curves of symmetric Li/Li cells with polymer and hybrid electrolytes at 0.6 mA cm⁻² and 55 °C. (c) AC impedance spectra of the Li/hybrid electrolyte/Li cell during galvanostatic cycling at 0.6 mA cm⁻² and 55 °C. (d) Interfacial resistances in symmetric Li/Li cells with different solid electrolytes during galvanostatic cycling.

voltammograms reveal that the anodic voltage limit of the hybrid electrolyte is higher than that of the polymer electrolyte. This suggests that the LLZAO membrane contributes to the improved electrochemical stability of the hybrid electrolyte. The hybrid electrolyte's superior oxidative stability makes it suitable for use with high-voltage cathodes in lithium metal battery systems.

TGA was conducted on both the polymer and hybrid electrolytes, as

shown in Fig. S5. Both the polymer and hybrid electrolytes exhibited weight loss starting around 260 $^{\circ}$ C, attributed to the decomposition of the polymer component within the solid electrolytes. The total weight losses at 800 $^{\circ}$ C were 94.3 % for the polymer electrolyte and 56.5 % for the hybrid electrolyte. The enhanced heat resistance of the hybrid electrolyte results from the presence of the robust, fibrous LLZAO ceramic membrane.

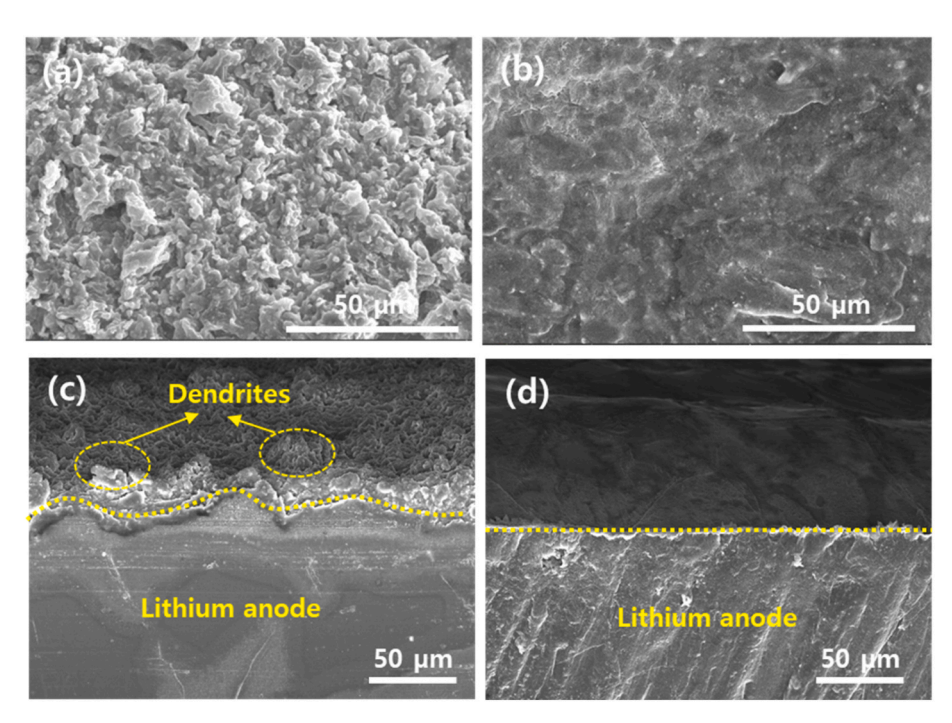


Fig. 5. SEM surface images of Li electrodes taken from disassembled symmetric lithium cells using (a) polymer electrolyte and (b) hybrid electrolyte after 150 h of cycling at 0.6 mA cm⁻² and 55 °C. SEM cross-sectional images of Li electrodes taken from disassembled symmetric lithium cells using (c) polymer electrolyte and (d) hybrid electrolyte after 150 h of cycling at 0.6 mA cm⁻² and 55 °C.

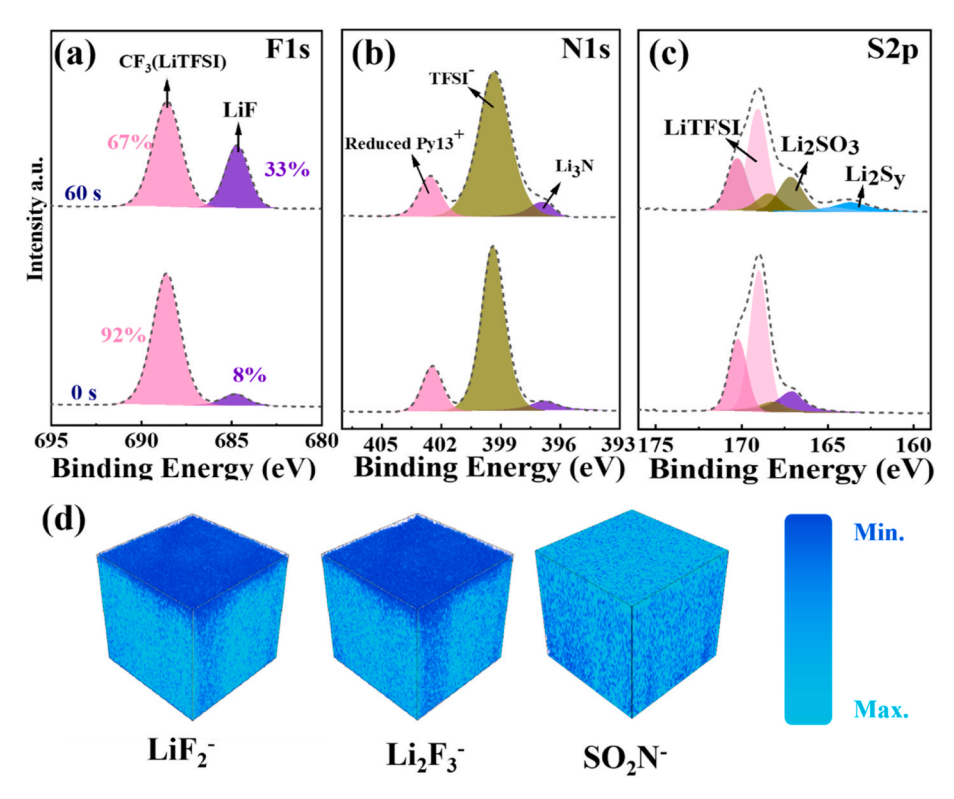


Fig. 6. (a) F 1s, (b) N 1s, and (c) S 2p XPS spectra of cycled Li electrodes with the Hybrid electrolyte. (d) Three-dimensional TOF-SIMS profiles and ion distribution maps of LiF_2^- , $Li_2F_3^-$, and SO_2N^- ion fragments at varying sputtering depths.

Fig. 4a shows the voltage behavior of symmetric Li cells incorporating different solid electrolytes, obtained by increasing the current density from 0.2 to 2.0 mA cm⁻² at 55 °C during galvanostatic deposition and stripping. For the polymer electrolyte, the polarization voltage increased gradually with current density until reaching 0.8 mA cm followed by a sharp voltage rise at 1.0 mA cm⁻², corresponding its critical current density (CCD). In contrast, the hybrid electrolyte exhibited a significant voltage increase at 2.0 mA cm⁻², suggesting that its CCD is twice that of the polymer electrolyte. To examine the lithium plating/stripping stability below the critical current density, the symmetric Li cells were subjected to galvanostatic cycling at $0.6~\mathrm{mA}~\mathrm{cm}^{-2}$ and 55 $^{\circ}$ C (Fig. 4b). An initial overpotential of 130 mV was observed in the symmetric Li cell with polymer electrolyte, increasing steadily to 3.0 V after 150 h of cycling. In contrast, the Li/hybrid electrolyte/Li cell exhibited a more stable overpotential, which increased only slightly to 148 mV even after 1000 h. This stable cycling behavior of the hybrid electrolyte cell can be attributed to its robust mechanical properties, leading to the mitigation of lithium dendrite growth. Additionally, the homogeneous and rapid Li⁺ ion flux facilitated by the fibrous LLZAO framework contributes to the long-term cycling of the hybrid electrolyte [43]. The Li/hybrid electrolyte/Li cell was also cycled at 25 °C. As shown in Fig. S6 and S7, the symmetric Li cell operated stably at 0.1 mA cm⁻² for 1000 h without short-circuiting, and the CCD reached up to 0.5 mA cm⁻². These results demonstrate that the hybrid electrolyte also exhibits favorable cycling stability at room temperature. The symmetric Li/solid electrolyte/Li cells were subjected to AC impedance measurement to monitor interfacial resistances, providing insights into the stability at the lithium/solid electrolyte interface. Fig. 4c provides the AC impedance spectra of the hybrid electrolyte cell, and the corresponding interfacial resistances for the cells employing different solid electrolytes are presented in Fig. 4d. For the polymer electrolyte, the interfacial resistance markedly increased from 103.7 to 325.0 Ω after 150 h of cycling, indicating severe interfacial degradation. In contrast, the hybrid electrolyte cell exhibited only a slight increase in interfacial resistance, from 85.5 to 106.2 Ω even after 1000 h, demonstrating much greater

interfacial stability. The superior stability at the hybrid electrolyte/Li metal interface is attributed to the combined effects of high ionic conductivity and robust mechanical strength, which enable rapid ${\rm Li}^+$ transport across the interface, while effectively suppressing lithium dendrite growth.

Fig. 5a and b shows the top-view SEM images of lithium electrodes retrieved from the cycled Li/Li cells, while Fig. 5c and d presents their cross-sectional SEM images. A rough and dendritic morphology is observed on the Li surface after 150 h of cycling in the polymer electrolyte. In contrast, the Li electrode cycled in the hybrid electrolyte remains smooth and planar, owing to its enhanced mechanical integrity and the uniform Li deposition/stripping behavior, which collectively suppress the lithium dendrite growth.

To elucidate the chemical composition and evolution of the SEI, XPS measurements were performed on cycled lithium electrodes obtained from the hybrid electrolyte. As shown in Fig. 6a-c and S8, the SEI consists of both inorganic and organic species, including LiF (684.8 eV in F 1s), CF $_3$ groups from LiTFSI (688.6 eV in F 1s), reduced Pyr $_{13}$ (402.5 eV in N 1s), TFSI $^-$ fragments (399.4 eV in N 1s), Li₃N (396.8 eV in N 1s), Li_2CO_3 , and $\text{Li}_2\text{SO}_2/\text{Li}_2\text{S}_v$ [44,45]. Quantitative peak fitting confirms a depth-dependent enrichment of inorganic components. In the F 1s region (Fig. 6a), the LiF fraction increases from 8 % at the surface to 33 % after 60 s of etching, while the CF₃ contribution decreases accordingly. Similarly, in the Li 1s spectra (Fig. S8a), the LiF component increases from 35 % to 45 % upon sputtering, whereas Li₂CO₃ decreases from 78 % to 52 %. Li₂S_v signals are detected only after etching (Fig. 6c), suggesting that surface organic products initially mask these species. The Li₃N contribution (Fig. 6b) persists before and after etching and shows a slight increase with depth, consistent with its stable incorporation into the SEI. Full-survey XPS spectra (Fig. S9) further reveal that the atomic percentages of N and F increase after etching (Table S1), supporting the formation of an inorganic-rich inner layer. ToF-SIMS depth profiling (Fig. 6d) corroborates these findings, showing an accumulation of LiF-related fragments (LiF2, Li2F3) with depth, while SO2N intensity decreases, confirming the gradient structure of the SEI. Taken together,

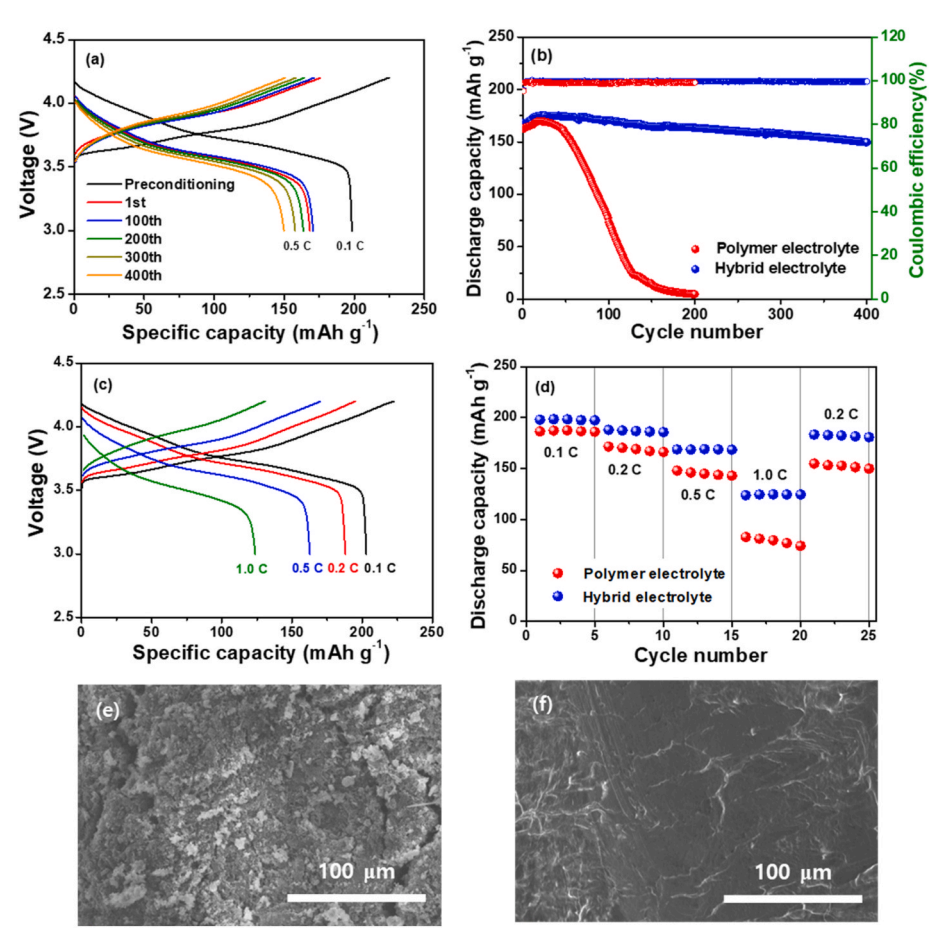


Fig. 7. (a) Voltage curves of the Li/hybrid electrolyte/NCM cell during cycling at 55 °C, and (b) comparison of cycling performance for Li/NCM cells employing different solid electrolytes at 0.5C and 55 °C. (c) Voltage profiles of the Li/hybrid electrolyte/NCM cell obtained at different current densities at 55 °C. (d) Rate performance of Li/NCM cells using different solid electrolytes at 55 °C. SEM images of lithium electrodes retrieved from Li/NCM cells with (e) polymer electrolyte and (f) hybrid electrolyte after 100 cycles.

these results indicate the formation of a dual-layer SEI: an organic-rich outer layer derived from electrolyte decomposition and an inorganic-rich inner layer dominated by LiF and Li $_3$ N. Functionally, Li $_3$ N provides fast Li $^+$ transport pathways, while LiF — with its high surface energy, low electronic conductivity, and facile Li $^+$ migration — suppresses parasitic reactions and dendrite formation [44]. Compared with the polymer electrolyte, the hybrid system containing LLZAO promotes the preferential formation of LiF and Li $_3$ N, yielding a more stable SEI. Although reductive decomposition of the ionic liquid (Pyr $_{13}$ -TFSI) may occur, the concurrent enrichment of inorganic species mitigates side reactions and ensures long-term cycling stability.

The Li/NCM cells (active mass loading: 6.1 mg cm⁻²) were assembled using different solid electrolytes, and their cycling performance was evaluated at 55 °C. During the first preconditioning cycle at 0.1C, the cell with the hybrid electrolyte delivered a high initial capacity of 198.3 $mAh g^{-1}$ (Fig. 7a), which is greater than the 186.5 $mAh g^{-1}$ recorded for the polymer electrolyte system (Fig. S10a). Following two initial preconditioning cycles at a rate of 0.1C, the Li/NCM cells were subsequently cycled at 0.5C. The resulting voltage profiles of the cells with hybrid electrolyte and polymer electrolyte during cycling are presented in Fig. 7a and Fig. S10a, respectively, and a comparison of the cycling performance between the two cells is presented in Fig. 7b. As depicted in figure, the capacity of the cell using the polymer electrolyte dropped to just 3.0 % of its initial value after 200 cycles. In contrast, the hybrid electrolyte-based cell demonstrated a high initial discharge capacity of 168.3 mAh g^{-1} and preserved 89.0 % of this capacity (149.8 mAh g^{-1}) after 400 cycles, along with maintaining a high coulombic efficiency of 99.97 % over the entire cycling. The enhanced cycling stability of the

cell employing the hybrid electrolyte can be attributed to its high electrochemical stability, favorable interfacial properties, and mechanical robustness, which collectively suppress the dendritic growth of lithium and side reactions at the interface. Fig. 7c and S10b show the chargedischarge profiles of cells employing the hybrid electrolyte and the polymer electrolyte across a range of C rates, with the corresponding rate capability summarized in Fig. 7d. As the C rate increases, both cells exhibit the expected decrease in discharge capacities, arising from increased polarization within the cell. Notably, at every tested C rate, the hybrid electrolyte cell maintains smaller overpotentials and higher capacity retention than the polymer electrolyte cell. This superior high rate performance is consistent with the hybrid electrolyte's higher ionic conductivity and lower interfacial resistance, which reduce the ohmic and charge transfer components of polarization and sustain rapid Li+ flux at the electrode/electrolyte interface. Mechanistically, the LLZAOreinforced hybrid electrolyte provides continuous Li+ conduction pathways and a more stable, low-impedance interface, allowing deeper utilization of active materials before reaching voltage limits. Consequently, the hybrid electrolyte cell exhibits superior performance throughout the entire range of C rates. Fig. 7e and f presents surface SEM images of the lithium anodes retrieved from the Li/NCM cells with polymer electrolyte and hybrid electrolyte after 100 cycles, respectively. As shown in the images, the lithium anode cycled in the polymer electrolyte exhibits a large number of lithium dendrites, which result from inhomogeneous lithium deposition and stripping. In contrast, the lithium anode in the hybrid electrolyte-based cell displays a smooth and dense surface. The favorable interfacial properties and high mechanical strength of the hybrid electrolyte promote uniform lithium deposition and stripping, thereby suppressing dendrite growth during cycling and leading to superior cycling performance. Fig. S11 shows the cycling stability of the Li/NCM cell with hybrid electrolyte at 0.2C and 25 $^{\circ}$ C. Although the initial discharge capacity at ambient temperature is lower than that at 55 $^{\circ}$ C, the cell maintains 129.2 mAh g $^{-1}$ after 300 cycles (88.3 % retention), followed by large capacity fading, indicating stable cycling behavior within this range.

To evaluate thermal safety, the open circuit voltage (OCV) of charged solid-state cells with different electrolytes was monitored at $160\,^{\circ}\text{C}$. As presented in Fig. S12, the hybrid electrolyte-based cell exhibited stable OCV behavior for up to $120\,\text{min}$. In contrast, the OCV of the polymer electrolyte-based cell dropped to $0\,\text{V}$ after 33 min, indicating short-circuit of the cell. Dimensional stability of the solid electrolytes was tested by maintaining them at $160\,^{\circ}\text{C}$ for $1\,\text{h}$. As illustrated in Fig. S13, the hybrid electrolyte mainta3ined its structural integrity and original size at $160\,^{\circ}\text{C}$. In contrast, the polymer electrolyte exhibited melting and significant thermal shrinkage, which resulted in short-circuit of the cell with polymer electrolyte. These results reveal that the use of the hybrid electrolyte significantly enhances the thermal safety of the Li/NCM cells.

4. Conclusions

In our study, we prepared a mechanically robust hybrid electrolyte reinforced with a three-dimensional fibrous LLZAO membrane. The incorporation of LLZAO nanofibers provided continuous and efficient lithium-ion conduction pathways while enhancing the mechanical integrity compared to polymer electrolytes. Owing to the synergistic effect between the inorganic and polymer components, the hybrid electrolyte exhibited high ionic conductivity, improved electrochemical stability, and good interfacial compatibility with the lithium electrode. As a result, the symmetric Li/Li cells employing the hybrid electrolyte exhibited stable cycling over a period of 1000 h, with no notable increase in overpotential or evidence of short-circuiting caused by dendritic lithium growth. The Li/NCM solid-state cell incorporating the hybrid electrolyte exhibited a high initial capacity and retained 89.0 % of its capacity after 400 cycles at 0.5C and 55 °C, indicating outstanding cycling stability. Additionally, the high thermal stability of the LLZAObased hybrid electrolyte ensured safe operation without short-circuiting at 160 °C. Our results highlight the potential of the hybrid electrolyte as a solid-state electrolyte for high-performance all-solid-state lithium batteries (ASSLBs), offering long cycle life and enhanced safety.

CRediT authorship contribution statement

Lei Wu Tian: Writing – original draft, Investigation, Data curation, Conceptualization. Ji Wan Kim: Validation, Formal analysis, Data curation. Dongmei Xie: Methodology, Formal analysis, Data curation. Weihan Li: Validation, Methodology, Formal analysis. Dong-Won Kim: Writing – review & editing, Supervision, Project administration, Funding acquisition, Conceptualization.

Declaration of competing interest

The authors declare that they have no known competing financial interests or personal relationships that could have appeared to influence the work reported in this paper.

Acknowledgments

This study was financially supported by the National Research Foundation of Korea (NRF) grant funded by the Korean government (MSIT) (RS-2024-00454354) and the Technology Innovation Program (20023145), funded by the Ministry of Trade, Industry, and Energy (MOTIE, Korea). One of the authors (Leiwu Tian) acknowledges the support offered by the China Scholarship Council (202108260004).

Appendix A. Supplementary data

Supplementary data to this article can be found online at https://doi.org/10.1016/j.jpowsour.2025.238687.

Data availability

Data will be made available on request.

References

- M. Li, J. Lu, Z. Chen, K. Amine, 30 years of lithium-ion batteries, Adv. Mater. 30 (2018) e1800561, https://doi.org/10.1002/adma.201800561.
- [2] D. Lin, Y. Liu, Y. Cui, Reviving the lithium metal anode for high-energy batteries, Nat. Nanotechnol. 12 (2017) 194–206, https://doi.org/10.1038/nnano.2017.16.
- [3] J.W. Choi, D. Aurbach, Promise and reality of post-lithium-ion batteries with high energy densities, Nat. Rev. Mater. 1 (2016) 2058–8437, https://doi.org/10.1038/ natreymats.2016.13.
- [4] Q. Zhao, S. Stalin, C.-Z. Zhao, L.A. Archer, Designing solid-state electrolytes for safe, energy-dense batteries, Nat. Rev. Mater. 5 (2020) 229–252, https://doi.org/ 10.1038/s41578-019-0165-5.
- [5] Z. Gao, H. Sun, L. Fu, F. Ye, Y. Zhang, W. Luo, Y. Huang, Promises, challenges, and recent progress of inorganic solid-state electrolytes for all-solid-state lithium batteries, Adv. Mater. 30 (2018) e1705702, https://doi.org/10.1002/ adma.201705702
- [6] J.C. Bachman, S. Muy, A. Grimaud, H.H. Chang, N. Pour, S.F. Lux, O. Paschos, F. Maglia, S. Lupart, P. Lamp, L. Giordano, Y. Shao-Horn, Inorganic solid-state electrolytes for lithium batteries: mechanisms and properties governing ion conduction, Chem. Rev. 116 (2016) 140–162, https://doi.org/10.1021/acs.chemrev.5b00563.
- [7] B. Zhang, R. Tan, L. Yang, J. Zheng, K. Zhang, S. Mo, Z. Lin, F. Pan, Mechanisms and properties of ion-transport in inorganic solid electrolytes, Energy Storage Mater. 10 (2018) 139–159, https://doi.org/10.1016/j.ensm.2017.08.015.
- [8] A. Li, X. Liao, H. Zhang, L. Shi, P. Wang, Q. Cheng, J. Borovilas, Z. Li, W. Huang, Z. Fu, M. Dontigny, K. Zaghib, K. Myers, X. Chuan, X. Chen, Y. Yang, Nacreinspired composite electrolytes for load-bearing solid-state lithium-metal batteries, Adv. Mater. 32 (2020) e1905517, https://doi.org/10.1002/adma.201905517.
- [9] S. Li, Z. Yang, S.-B. Wang, M. Ye, H. He, X. Zhang, C.-W. Nan, S. Wang, Sulfide-based composite solid electrolyte films for all-solid-state batteries, Commun. Med. 5 (2024) 44, https://doi.org/10.1038/s43246-024-00482-8.
- [10] X. Zhang, S. Cheng, C. Fu, G. Yin, L. Wang, Y. Wu, H. Huo, Advancements and challenges in organic-inorganic composite solid electrolytes for all-solid-state lithium batteries, Nano-Micro Lett. 17 (2024) 2, https://doi.org/10.1007/s40820-024-01498-y.
- [11] Q. Zhou, J. Ma, S. Dong, X. Li, G. Cui, Intermolecular chemistry in solid polymer electrolytes for high-energy-density lithium batteries, Adv. Mater. 31 (2019) e1902029, https://doi.org/10.1002/adma.201902029.
- [12] Z. Li, J. Fu, X. Zhou, S. Gui, L. Wei, H. Yang, H. Li, X. Guo, Ionic conduction in polymer-based solid electrolytes, Adv. Sci. 10 (2023) e2201718, https://doi.org/ 10.1002/advs.202201718.
- [13] X. Huang, T. Li, W. Fan, R. Xiao, X.B. Cheng, Challenges and solutions of solid-state electrolyte film for large-scale applications, Adv. Energy Mater. 14 (2024) 2303850, https://doi.org/10.1002/aenm.202303850.
- [14] J. Sheng, Q. Zhang, C. Sun, J. Wang, X. Zhong, B. Chen, C. Li, R. Gao, Z. Han, G. Zhou, Crosslinked nanofiber-reinforced solid-state electrolytes with polysulfide fixation effect towards high safety flexible lithium-sulfur batteries, Adv. Funct. Mater. 32 (2022) 2203272, https://doi.org/10.1002/adfm.202203272.
- [15] X. Yu, A. Manthiram, A review of composite polymer-ceramic electrolytes for lithium batteries, Energy Storage Mater. 34 (2021) 282–300, https://doi.org/ 10.1016/j.ensm.2020.10.006.
- [16] Y. Zhao, L. Wang, Y. Zhou, Z. Liang, N. Tavajohi, B. Li, T. Li, Solid polymer electrolytes with high conductivity and transference number of li ions for Li-based rechargeable batteries, Adv. Sci. 8 (2021) 2003675, https://doi.org/10.1002/ advs.202003675.
- [17] G. Zhou, F. Li, H.-M. Cheng, Progress in flexible lithium batteries and future prospects, Energy Environ. Sci. 7 (2014) 1307–1338, https://doi.org/10.1039/ c3ce42182g
- [18] L. Tian, J.-W. Kim, D.-W. Kim, Solid hybrid electrolytes based on conductive oxides and polymer electrolytes for all-solid-lithium batteries, Mater. Chem. Front. 5 (2024) 455. https://doi.org/10.1039/d3om00736g.
- [19] S. Liu, W. Liu, D. Ba, Y. Zhao, Y. Ye, Y. Li, J. Liu, Filler-integrated composite polymer electrolyte for solid-state lithium batteries, Adv. Mater. 35 (2023) e2110423. https://doi.org/10.1002/adma.202110423.
- [20] J. Wang, S. Guo, Z. Li, W. Kou, J. Zhu, J. Dang, Y. Zhang, W. Wu, Highly conductive thin composite solid electrolyte with vertical Li₇La₃Zr₂O₁₂ sheet arrays for high-energy-density all-solid-state lithium battery, Chem. Eng. J. 450 (2022) 137994, https://doi.org/10.1016/j.cej.2022.137994.
- [21] C. Liu, J. Wang, W. Kou, Z. Yang, P. Zhai, Y. Liu, W. Wu, J. Wang, A flexible, ion-conducting solid electrolyte with vertically bicontinuous transfer channels toward high performance all-solid-state lithium batteries, Chem. Eng. J. 404 (2021) 126517. https://doi.org/10.1016/j.cej.2020.126517.
- [22] M. Gong, Y. Liang, K. Li, C. Guo, X. Zhao, J. Liang, Y. Huang, M. Zhao, Y. Dong, Y. Ren, D. Zhuang, C.-W. Nan, Q. Gong, Solvent volume expansion inhibition

- during freeze casting and its application in composite solid lithium electrolytes, Nano Energy 118 (2023) 108968, https://doi.org/10.1016/j.
- [23] Y. Ma, J. Wu, H. Xie, R. Zhang, Y. Zhang, E. Liu, N. Zhao, C. He, A.B. Wong, The synthesis of three-dimensional hexagonal boron nitride as the reinforcing phase of polymer-based electrolyte for all-solid-state li metal batteries, Angew Chem. Int. Ed. Engl. 63 (2024) e202317256, https://doi.org/10.1002/anie.202317256.
- [24] P. Fan, H. Liu, V. Marosz, N.T. Samuels, S.L. Suib, L. Sun, L. Liao, High performance composite polymer electrolytes for lithium-ion batteries, Adv. Funct. Mater. 31 (2021) 2101380, https://doi.org/10.1002/adfm.202101380.
- [25] S. Li, S.Q. Zhang, L. Shen, Q. Liu, J.B. Ma, W. Lv, Y.B. He, Q.H. Yang, Progress and perspective of ceramic/polymer composite solid electrolytes for lithium batteries, Adv. Sci. 7 (2020) 1903088, https://doi.org/10.1002/advs.201903088.
- [26] M. Liu, S. Zhang, E.R.H. van Eck, C. Wang, S. Ganapathy, M. Wagemaker, Improving Li-ion interfacial transport in hybrid solid electrolytes, Nat. Nanotechnol. 17 (2022) 959–967, https://doi.org/10.1038/s41565-022-01162-9.
- [27] W. Wu, Z. Wei, J. Wang, J. Shang, M. Wang, S.-S. Chi, Q. Wang, L. Du, T. Zhang, Z. Zheng, Y. Deng, Enabling high-energy flexible solid-state lithium ion batteries at room temperature, Chem. Eng. J. 424 (2021) 130335, https://doi.org/10.1016/j.cei.2021.130335
- [28] H.R. Wang, Y.N. Yang, F. Bai, T. Zhang, Anion-decoordination cell formation process stabilizes dual electrodes for long-life quasi-solid-state lithium metal battery, Adv. Mater. Interfac. 9 (2021) 2101840, https://doi.org/10.1002/ admi/202101840
- [29] C. Deng, N. Chen, C. Hou, H. Liu, Z. Zhou, R. Chen, Enhancing interfacial contact in solid-state batteries with a gradient composite solid electrolyte, Small 17 (2021) e2006578. https://doi.org/10.1002/smll.202006578.
- [30] L.W. Tian, J.W. Kim, S.-B. Hong, H.-H. Ryu, U.-H. Kim, Y.-K. Sun, D.-W. Kim, All-solid-state lithium batteries featuring hybrid electrolytes based on Li⁺ ion-conductive Li₂La₃Zr₂O₁₂ framework and full-concentration gradient Ni-rich NCM cathode, Chem. Eng. J. 450 (2022) 138043, https://doi.org/10.1016/j.cei.2022.138043.
- [31] L.W. Tian, J. Kim, D.-W. Kim, Solid hybrid electrolyte featuring a vertically aligned Li_{6.4}La_{3.0}Zr_{1.4}Ta_{0.6}O_{1.2} membrane for all-solid-state lithium batteries, ACS Appl. Mater. Interfaces 15 (2023) 33541–33549, https://doi.org/10.1021/ acsami.3c04131.
- [32] Y. Seo, Y.-C. Jung, M.-S. Park, D.-W. Kim, Solid polymer electrolyte supported by porous polymer membrane for all-solid-state lithium batteries, J. Membr. Sci. 603 (2020) 117995, https://doi.org/10.1016/j.memsci.2020.117995.
- [33] J. Yan, Y. Zhao, X. Wang, S. Xia, Y. Zhang, Y. Han, J. Yu, B. Ding, Polymer template synthesis of soft, light, and robust oxide ceramic films, iScience 15 (2019) 185–195, https://doi.org/10.1016/j.isci.2019.04.028.
- [34] Y. Li, W. Zhang, Q. Dou, K.W. Wong, K.M. Ng, Li₇La₃Zr₂O₁₂ ceramic nanofiber-incorporated composite polymer electrolytes for lithium metal batteries, J. Mater. Chem. A 7 (2019) 3391–3398, https://doi.org/10.1039/c8ta11449h.

- [35] S. Song, X. Qin, Y. Ruan, W. Li, Y. Xu, D. Zhang, J. Thokchom, Enhanced performance of solid-state lithium-air batteries with continuous 3D garnet network added composite polymer electrolyte, J. Power Sources 461 (2020) 228146, https://doi.org/10.1016/j.jpowsour.2020.228146.
- [36] P. Pan, M. Zhang, Z. Cheng, L. Jiang, J. Mao, C. Ni, Q. Chen, Y. Zeng, Y. Hu, K. Fu, Garnet ceramic fabric-reinforced flexible composite solid electrolyte derived from silk template for safe and long-term stable all-solid-state lithium metal batteries, Energy Storage Mater. 47 (2022) 279–287, https://doi.org/10.1016/j. ensm 2022 02 018
- [37] G. Wang, H. Liu, Y. Liang, C. Wang, L.-Z. Fan, Composite polymer electrolyte with three-dimensional ion transport channels constructed by NaCl template for solidstate lithium metal batteries, Energy Storage Mater. 45 (2022) 1212–1219, https:// doi.org/10.1016/j.ensm.2021.11.021.
- [38] D. Yu, Z. Ma, Z. Liu, X. Jiang, H.A. Younus, X. Wang, S. Zhang, Optimizing interfacial wetting by ionic liquid for high performance solid-state lithium metal batteries operated at ambient temperature, Chem. Eng. J. 457 (2023) 141043, https://doi.org/10.1016/j.cej.2022.141043.
- [39] Y. Zhai, W. Hou, M. Tao, Z. Wang, Z. Chen, Z. Zeng, X. Liang, P. Paoprasert, Y. Yang, N. Hu, S. Song, Enabling high-voltage "superconcentrated ionogel-inceramic" hybrid electrolyte with ultrahigh ionic conductivity and single Li⁺-ion transference number, Adv. Mater. 34 (2022) e2205560, https://doi.org/10.1002/ adma.202205560.
- [40] M.J. Lee, D.O. Shin, J.Y. Kim, J. Oh, S.H. Kang, J. Kim, K.M. Kim, Y.M. Lee, S. O. Kim, Y.-G. Lee, Interfacial barrier free organic-inorganic hybrid electrolytes for solid state batteries, Energy Storage Mater. 37 (2021) 306–314, https://doi.org/10.1016/j.ensm.2021.02.013.
- [41] N. Wu, P.H. Chien, Y. Qian, Y. Li, H. Xu, N.S. Grundish, B. Xu, H. Jin, Y.Y. Hu, G. Yu, J.B. Goodenough, Enhanced surface interactions enable fast Li⁺ conduction in oxide/polymer composite electrolyte, Angew Chem. Int. Ed. Engl. 59 (2020) 4131–4137, https://doi.org/10.1002/anie.201914478.
- [42] P. Ranque, J. Zagorski, S. Devaraj, F. Aguesse, J.M. Lopez del Amo, Characterization of the interfacial Li-ion exchange process in a ceramic-polymer composite by solid state NMR, J. Mater. Chem. A 9 (2021) 17812–17820, https://doi.org/10.1039/d1ta03720j.
- [43] Y. Zhao, J. Yan, W. Cai, Y. Lai, J. Song, J. Yu, B. Ding, Elastic and well-aligned ceramic LLZAO nanofiber based electrolytes for solid-state lithium batteries, Energy Storage Mater. 23 (2019) 306–313, https://doi.org/10.1016/j. ensm.2019.04.043.
- [44] K. Zhang, F. Wu, X. Wang, S. Weng, X. Yang, H. Zhao, R. Guo, Y. Sun, W. Zhao, T. Song, X. Wang, Y. Bai, C. Wu, 8.5 μm-thick flexible-rigid hybrid solid-electrolyte/lithium integration for air-stable and interface-compatible all-solid-state lithium metal batteries, Adv. Energy Mater. 12 (2022) 2200368, https://doi.org/10.1002/aenm.202200368.
- [45] W. Li, U.H. Kim, A. Dolocan, Y.K. Sun, A. Manthiram, Formation and inhibition of metallic lithium microstructures in lithium batteries driven by chemical crossover, ACS Nano 11 (2017) 5853–5863, https://doi.org/10.1021/acsnano.7b01494.